IEEE Access
Multidisciplinary | Rapid Review | Open Access Journal

Received June 27, 2021, accepted July 18, 2021, date of publication September 8, 2021, date of current version September 14, 2021.

Digital Object Identifier 10.1109/ACCESS.2021.3105594

Target Detection Through Riemannian Geometric Approach With Application to Drone Detection

HOSSEIN CHAHROUR[1], (Student Member, IEEE), RICHARD M. DANSEREAU[1], (Senior Member, IEEE), SREERAMAN RAJAN[1], (Senior Member, IEEE), AND BHASHYAM BALAJI[2], (Senior Member, IEEE)

[1]Department of Systems and Computer Engineering, Carleton University, Ottawa, ON K1S 5B6, Canada
[2]Radar Sensing and Exploitation Section, Defence Research and Development Canada, Ottawa, ON K1A 0Z4, Canada

Corresponding author: Hossein Chahrour (chahrour@sce.carleton.ca)

This work was supported and funded in part by the Natural Sciences and Engineering Council (NSERC), and in part by the Defence Research and Development Canada.

ABSTRACT Radar detection of small drones in presence of noise and clutter is considered from a differential geometry viewpoint. The drone detection problem is challenging due to low radar cross section (RCS) of drones, especially in cluttered environments and when drones fly low and slow in urban areas. This paper proposes two detection techniques, the Riemannian-Brauer matrix (RBM) and the angle-based hybrid-Brauer (ABHB), to improve the probability of drone detection under small sample size and low signal-to-clutter ratio (SCR). These techniques are based on the regularized Burg algorithm (RBA), the Brauer disc (BD) theorem, and the Riemannian mean and distance. Both techniques exploit the RBA to obtain a Toeplitz Hermitian positive definite (THPD) covariance matrix from each snapshot and apply the BD theorem to cluster the clutter-plus-noise THPD covariance matrices. The proposed Riemannian-Brauer matrix technique is based on the Riemannian distance between the Riemannian mean of clutter-plus-noise cluster and potential targets. The proposed angle-based hybrid-Brauer technique uses the Euclidean tangent space and the Riemannian geodesical distances between the Riemannian mean, the Riemannian median and the potential target point. The angle at the potential target on the manifold is computed using the law of cosines on the manifold. The proposed detection techniques show advantage over the fast Fourier transform, the Riemannian distance-based matrix and the Kullback-Leibler (KLB) divergence detectors. The validity of both proposed techniques are demonstrated with real data.

INDEX TERMS Differential geometry, Burg algorithm, Brauer disc theorem, Riemannian mean and distance, Toeplitz Hermitian positive definite covariance matrices.

I. INTRODUCTION

Radar target detection in the presence of clutter and noise under low signal-to-noise ratio (SNR) is an important and evolving problem in signal processing [1]. Specifically, the detection of small drones presents more challenging factors, such as low radar cross section (RCS), low altitude flying in cluttered environment and slow flying in urban areas. These factors reduce the SNR and limit the number of received radar snapshots and result in low probability of detection.

The associate editor coordinating the review of this manuscript and approving it for publication was Seung-Hyun Kong.

The drone detection problem has been studied by many researchers. The detection technique introduced by [2] exploits a passive coherent location (PCL) radar system for the detection of the micro-Doppler signature induced by the blades of the drone. The micro-Doppler characteristics of the drone are extracted from the cross-ambiguity function map. Another drone detection technique presented by [3] is based on an ultra-wide band sensing system and advanced signal processing methods. This technique has many advantages, such as sensing small drones built from heterogeneous materials and detecting a drone's movements in out of sight scenarios.

Current signal processing techniques may be inadequate to reliably capture small or mini drones because they do move

very fast. The amount of data available for processing may be very small and therefore some advanced signal processing techniques may be in order. The probability of drone detection can be improved with sophisticated signal processing algorithms. Classical detection schemes like the fast Fourier transform (FFT) constant false alarm rate (CFAR) [4] detector suffer from performance degradation due to small number of snapshots and poor Doppler resolution. Target detection with small amount of data can be approached from the geometrical point of view. In particular, differential geometry can be used to provide better detection performance by exploiting distance and angle metrics [5], [6].

Information geometry constitutes a framework that considers probability densities as structure of differential geometry [5]. Specifically, in Riemannian geometry [7], each density function parameterized by a Toeplitz Hermitian positive definite (THPD) covariance matrix representing a point on the statistical Riemannian manifold [8], [9]. Using the Karcher Barycenter [10], the Riemannian (geometric) mean of THPD covariance matrices can be calculated and the Riemannian distance between two THPD covariance matrices, which is the shortest distance between two points of the manifold, can be computed.

There are many methods such as the Burg algorithm (BA) and the regularized Burg algorithm (RBA) [11], the atomic-norm minimization [12] and the nuclear-norm minimization [13] that can be used to estimate the THPD covariance matrix using a single snapshot. Both the atomic-norm and the nuclear-norm minimizations use the sample covariance matrix as an estimate for the covariance matrix and may suffer degradation when the number of snapshots are very limited. On the other hand, BA estimates the reflection coefficients by minimizing the average of the forward and backward linear prediction errors with high resolution. The RBA has a regularization parameter that adds more stability, provides better estimates of the reflection coefficients and guarantees a THPD covariance matrix. The RBA can be exploited to estimate the reflection coefficients for every snapshot of the radar observation data. From the reflection coefficients, one can estimate the THPD covariance matrix for each radar snapshot.

The Toeplitz structure of the covariance matrices are usually generated from a uniform linear array configuration [14], which can be exploited in improving target detection in the Riemannian space. There are many spectral properties that can be exploited in processing Toeplitz covariance matrices. Other array configurations may generate non-Toeplitz covariance matrices. While RBA estimates a THPD covariance matrix for every snapshot regardless of the antenna configurations, considering a uniform linear array for target detection may be a natural choice as covariance estimates of uniform linear array configuration are naturally THPD. This paper focuses only on uniform linear array configuration.

Localization of eigenvalues for square matrices can be used to establish a cluster bound around the maximum eigenvalues. Many eigenvalue inclusion techniques, such as the Gershgorin disc (GD) theorem [15], [16] and the Brauer disc (BD) theorem [17], [18], have been proposed to establish inclusion regions for the eigenvalues of square matrices. For THPD covariance matrices, all Gershgorin and Brauer discs have the same disc centre and generate overlapping discs with the largest eigenvalue associated with the largest GD and BD discs. The BD theorem is based on both the row and column summations, which provides a tighter disc bound on the eigenvalues in comparison with the GD theorem [18].

Signal detection based on information geometry was first introduced in 1989 and highlighted the importance of manifold theory in statistical information [5], [19] where the hypothesis testing problem was explained using a statistical manifold [6]. A novel signal detector based on a Riemannian manifold of Hermitian positive definite matrices, also known as the Riemannian distance (RD) based CFAR detector (RD-CFAR), was proposed by [20]–[23]. The RD-CFAR detector is based on the Riemannian mean or the Riemannian median of the reference covariance matrices around the covariance matrix under test. The Riemannian distance is computed between the covariance matrix under test and the Riemannian mean or median and then compared to a set threshold. Although, the RD-CFAR detector outperforms the traditional FFT-CFAR detector [24], it has two major drawbacks: the number of Riemannian mean or median computations is proportional to the number of snapshots and the Riemannian mean and median are not robust to outliers [25]. Another Riemannian geometry detection method was proposed in [25], [26] based on the Kullback-Leibler (KLB) divergence. The KLB technique performs better than the RD-CFAR detector and adaptive matched filter CFAR detectors, however the KLB mean and median are also not robust to outliers [26].

Two new detectors, the Riemannian-Brauer matrix (RBM) CFAR and the angle-based hybrid Brauer (ABHB) CFAR detectors are proposed in this paper. Both detectors have two stages in their implementation. RBM-CFAR and ABHB-CFAR detectors exploit the BD theorem to establish BD cluster bound for the clutter-plus-noise THPD covariance matrices and identify potential target points. In addition, they take advantage of the Riemannian metrics, such as distance and angle, and the Euclidean tangent space at potential THPD target point to improve the probability of detection. The proposed CFAR detectors provide 2–5 dB signal-to-clutter improvement over the FFT-CFAR, the RD-CFAR and the KLB-CFAR detectors when tested on simulated and real data.

The rest of the paper is organized as follows. Section II formulates and explains the radar detection problem. Section III provides a brief background on the Burg algorithm and the Riemannian space of THPD covariance matrices. Section IV presents the Gershgorin disc theorem and the Brauer disc theorem. Section V is devoted to the new proposed detection techniques, which are the primary contributions of this paper. Section VI and VII provide results obtained through simulations and real data analysis. Finally, Section VIII concludes the paper and gives some direction for future work.

II. DETECTION PROBLEM FORMULATION

The received complex radar data for an N element snapshot can be written as $\mathbf{x} = (x_0, \ldots, x_{N-1})$ and is realized as a multivariate stationary complex Gaussian process with zero mean, $\mathbf{x} \sim \mathcal{CN}(0, \mathbf{R})$, which can be written as

$$P(\mathbf{x}|\mathbf{R}) = \frac{1}{\sqrt{\pi^N \det(\mathbf{R})}} \exp(-\mathbf{x}^H \mathbf{R}^{-1} \mathbf{x}) \tag{1}$$

where $P(\mathbf{x}|\mathbf{R})$ is the probability density function (pdf) of a circular Gaussian random vector and $\mathbf{R}$ is a THPD covariance matrix.

In general, the detection problem can be formulated as the binary hypothesis testing problem [27], [28]

$$\begin{cases} H_0 : \mathbf{x} = \mathbf{n} + \mathbf{c} \\ H_1 : \mathbf{x} = \mathbf{s} + \mathbf{n} + \mathbf{c} \end{cases} \tag{2}$$

where $\mathbf{s}$ is a complex Gaussian random signal, $\mathbf{n}$ is complex Gaussian noise and $\mathbf{c}$ is complex valued Weibull clutter. As a special case, the Weibull clutter has a Gaussian PDF when the skewness parameter is 2 [29]. Under the null hypothesis H_0, the received snapshot consists of only noise-plus-clutter and under the alternative hypothesis H_1, the received snapshot contains the target in addition to the noise and clutter. The covariance matrix of the snapshot $\mathbf{x}$ can be determined using the Burg algorithm discussed in the next section.

III. REGULARIZED BURG ALGORITHM AND SPACE OF POSITIVE DEFINITE COVARIANCE MATRICES

Burg's method for maximum entropy spectral analysis plays a key role in spectral estimation, speech processing and radar covariance matrix estimation [11], [30]. The RBA will be exploited to estimate the reflection coefficients for every snapshot (range cell) of the radar observation data. From the reflection coefficients, one can estimate the THPD covariance matrix for each radar snapshot. Each THPD covariance matrix represents a convex cone residing on the Riemannian manifold, which can be manipulated using Riemannian metrics.

A. REGULARIZED BURG ALGORITHM

The regularized Burg algorithm is an alternative Bayesian composite model approach to spectral estimation. The reflection coefficients are based on autoregressive model order and minimizing the sum of mean squared values of the forward and backward prediction errors. This algorithm maintains a lattice structure, which provides robustness against coefficient value perturbation and less round-off noise [22]. The RBA is shown in Algorithm 1 [11], [21], [31], where ψ_1 is the regularization parameter and N is the number of reflection coefficients and autoregressive model order.

The reflection coefficients μ_k are used to calculate the r_k, which are the elements of the THPD covariance matrix $\mathbf{R}$ of

Algorithm 1 Regularized Burg Algorithm [20]

Initialization

$$f_0(k) = \mathbf{x}(k), \quad k = 0, \ldots, N-1,$$
$$b_0(k) = \mathbf{x}(k),$$
$$P_0 = \frac{1}{N} \sum_{k=0}^{N-1} |\mathbf{x}(k)|^2$$

for $n = 1$ to $N-1$ **do**

$$\mu_n = -\frac{\frac{2}{N-n} \sum_{k=n+1}^{N} f_{n-1}(k) \bar{b}_{n-1}(k-1) + \delta_n}{\frac{1}{N-n} \sum_{k=n+1}^{N} \left\{ |f_{n-1}(k)|^2 + |b_{n-1}(k-1)|^2 \right\} + \delta_d},$$

with

$$\nu_k^{(n)} = \psi_1 (2\pi)^2 (k-n)^2,$$
$$\delta_n = 2 \sum_{k=1}^{n-1} \nu_k^{(n)} a_k^{(n-1)} a_{n-k}^{(n-1)},$$
$$\delta_d = 2 \sum_{k=0}^{n-1} \nu_k^{(n)} |a_k^{(n-1)}|^2$$

and

$$\begin{cases} a_0^{(n)} = 1, \\ a_k^{(n)} = a_k^{(n-1)} + \mu_n \bar{a}_{n-k}^{(n-1)}, \quad k = 1, \ldots, n-1 \\ a_n^{(n)} = \mu_n \end{cases}$$

$$\begin{cases} f_n(k) = f_{n-1}(k) + \mu_n b_{n-1}(k-1), \\ b_n(k) = b_{n-1}(k-1) + \bar{\mu}_n f_{n-1}(k). \end{cases}$$

end for

snapshot $\mathbf{x}$ written as

$$\mathbf{R} = \begin{bmatrix} r_0 & \bar{r}_1 & \cdots & \bar{r}_{N-1} \\ r_1 & r_0 & \cdots & \bar{r}_{N-2} \\ \vdots & \ddots & \ddots & \vdots \\ r_{N-2} & \ddots & \ddots & \bar{r}_1 \\ r_{N-1} & \cdots & r_1 & r_0 \end{bmatrix}. \tag{3}$$

where $\bar{r}_1$ denotes the complex conjugate of r_1. The r_k are computed using [20]

$$r_0 = P_0, \quad r_1 = -P_0 \mu_1 \tag{4}$$
$$r_k = -P_{k-1} \mu_k \boldsymbol{\alpha}_{k-1}^T \mathbf{J}_{k-1} \mathbf{R}_{k-1}^{-1} \boldsymbol{\alpha}_{k-1}, \quad 2 \leqslant k \leqslant N-1 \tag{5}$$

where

$$\boldsymbol{\alpha}_{k-1} = \begin{bmatrix} r_1 \\ \vdots \\ r_{k-1}, \end{bmatrix}, \quad \mathbf{J}_0 = 1, \ \mathbf{J}_1 = \begin{bmatrix} 0 & 1 \\ 1 & 0 \end{bmatrix},$$

$$\mathbf{J}_{k-1} = \begin{bmatrix} 0 & 0 & \cdots & 1 \\ 0 & \cdots & 1 & 0 \\ & \cdots & \cdots & \\ 1 & \cdots & 0 & 0 \end{bmatrix},$$

$$\mathbf{R}_{k-1} = \mathbf{R}(2:k, 1:k-1), \quad P_{k-1} = P_0 \prod_{i=1}^{k-1}(1-|\mu_i|^2).$$

B. SPACE OF POSITIVE DEFINITE COVARIANCE MATRICES

The space of positive definite covariance matrices, also known as a Riemannian manifold, consists of a topological space with some similarity to a Euclidean space. Every point on the Riemannian manifold has a neighbourhood for which there exists a homeomorphism. A Riemannian manifold is a differentiable manifold in which each tangent space has an inner product that varies smoothly from point to point [32], [33]. Each point on the Riemannian manifold is a THPD covariance matrix $\mathbf{R}$ that belongs to a convex symmetric cone $\mathcal{M}$ residing on the manifold

$$\mathcal{M} = \{\mathbf{R} \mid \mathbf{R} \in \mathbb{P}, \mathbf{R} \succ 0\} \tag{6}$$

where $\succ$ denotes positive definite matrix, $\mathbb{P} = \left\{\mathbf{R}, \mathbf{R}^H = \mathbf{R}\right\}$ denotes the space of all Hermitian matrices and the quadratic form of $\mathbf{R}$ is $a^H\mathbf{R}a > 0, \forall a \in \mathbb{C}^n$. The process of acquiring a Riemannian mean (geometric) of K THPD matrices is an iterative gradient algorithm also known as Karcher Barycenter algorithm [31], which is based on the Jacobi field and exponential map

$$\mathbf{A}_{t+1} = \mathbf{A}_t^{1/2}\exp\left\{\epsilon \sum_{k=1}^{K} \operatorname{logm}(\mathbf{A}_t^{-1/2}\mathbf{R}_k\mathbf{A}_t^{-1/2})\right\}\mathbf{A}_t^{1/2} \tag{7}$$

where t is the iteration index, ϵ is the step size, logm is the Riemannian logarithmic map operator, K is the number of snapshots, $\{\mathbf{R}_1, \ldots, \mathbf{R}_K\}$ is a set of THPD matrices, $\mathbf{A}_1$ is the arithmetic mean of the THPD matrices and the converged $\mathbf{A}_{t+1}$ is the Riemannian mean $\mathbf{R}_{rm}$. Figure 1 illustrates an example of THPD covariance matrices and their Riemannian mean on a Riemannian manifold. Similarly, the Riemannian median can be defined using the same parameters as the Riemannian mean [34], which is given as

$$\mathbf{A}_{t+1} = \mathbf{A}_t^{1/2}\exp\left\{\epsilon \sum_{k=1}^{K} \frac{\operatorname{logm}(\mathbf{A}_t^{-1/2}\mathbf{R}_k\mathbf{A}_t^{-1/2})}{C}\right\}\mathbf{A}_t^{1/2} \tag{8}$$

where $C = \left\|\operatorname{logm}(\mathbf{A}_t^{-1/2}\mathbf{R}_k\mathbf{A}_t^{-1/2})\right\|_F$, $\|\cdot\|_F$ is the Frobenius norm and the converged $\mathbf{A}_{t+1}$ is the Riemannian median $\mathbf{R}_{rmed}$.

Another important metric for a Riemannian manifold is the Riemannian distance. The Riemannian distance is the minimum geodesical distance d_{R} between two THPD covariance matrices $\mathbf{R}_1$ and $\mathbf{R}_2$, that represent two points on the Riemannian manifold, and is defined by [7]

$$d_{\mathrm{R}}^2(\mathbf{R}_1, \mathbf{R}_2) = \left\|\operatorname{logm}(\mathbf{R}_1^{-1/2}\mathbf{R}_2\mathbf{R}_1^{-1/2})\right\|_F^2 = \sum_{k=1}^{l} \log^2(\lambda_k) \tag{9}$$

where $\{\lambda_1, \ldots, \lambda_l\}$ are the eigenvalues of $\mathbf{R}_1^{-1/2}\mathbf{R}_2\mathbf{R}_1^{-1/2}$ and l is the number of eigenvalues.

In addition, a tangent space can be defined for every point on the Riemannian manifold. A tangent vector $\mathbf{V}$ of the point

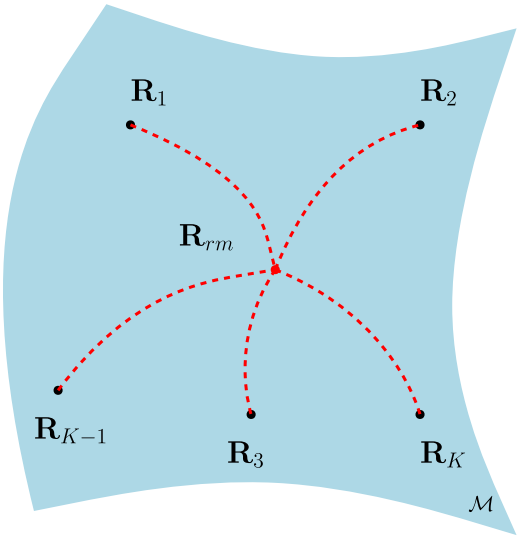

FIGURE 1. THPD matrices $\{\mathbf{R}_1, \mathbf{R}_2, \ldots, \mathbf{R}_K\}$ with Riemannian mean $\mathbf{R}_{rm}$ on Riemannian manifold $\mathcal{M}$.

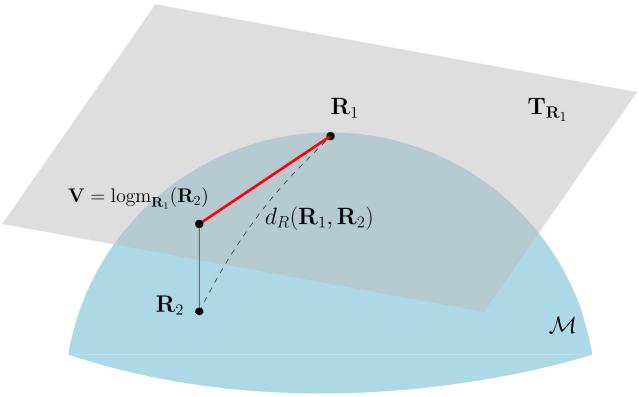

FIGURE 2. Projection of $\mathbf{R}_2$ onto the tangent space of $\mathbf{R}_1$.

$\mathbf{R}_2$ on the tangent space $\mathbf{T}_{R_1}$ is the projection of the point $\mathbf{R}_2$ onto the tangent space $\mathbf{T}_{R_1}$ as shown in Fig. 2. The projection is defined using the Riemannian logarithmic map operator [35] as

$$\begin{aligned}\mathbf{V} &= \operatorname{logm}_{\mathbf{R}_1}(\mathbf{R}_2) \\ &= \mathbf{R}_1^{1/2}\operatorname{logm}\left(\mathbf{R}_1^{-1/2}\mathbf{R}_2\mathbf{R}_1^{-1/2}\right)\mathbf{R}_1^{1/2}.\end{aligned} \tag{10}$$

Furthermore, the projection back to the space of the THPD covariance matrices can be done using the affine-invariant metric of (9) and the Riemannian exponential map operator expm as given below

$$\begin{aligned}\mathbf{R}_2 &= \operatorname{expm}_{\mathbf{R}_1}(\mathbf{V}) \\ &= \mathbf{R}_1^{1/2}\operatorname{expm}\left(\mathbf{R}_1^{-1/2}\mathbf{V}\mathbf{R}_1^{-1/2}\right)\mathbf{R}_1^{1/2}.\end{aligned} \tag{11}$$

The concept of tangent space can be used to manipulate THPD covariance matrices in Euclidean space where angles between projected THPD matrices can be calculated.

IV. GERSHGORIN DISC FOR TOEPLITZ MATRICES

The Gershgorin disc theorem is a well-known and efficient method for determining the inclusion domain of the eigenvalues of a matrix in terms of its entries. All eigenvalues of a matrix must lie in a union of discs, each centred at a diagonal element of the matrix and having a radius equal to the corresponding deleted row sum [36]. The Gershgorin disc theorem can also be applied to Toeplitz matrices.

Theorem 1 (Gershgorin Disc Theorem [17]): Let $\mathbf{R} = [r_{ij}] \in \mathbb{C}^{n\times n}$ be a Toeplitz matrix, $r_{ii} = r_0, n \geqslant 2$ and $\sigma(\mathbf{R})$ be the spectrum of $\mathbf{R}$. Then,

$$\begin{aligned}
\sigma(\mathbf{R}) \subseteq \Gamma(\mathbf{R}) &= \bigcup_{i=1}^{\lceil \frac{n}{2} \rceil} \Gamma_i(\mathbf{R}) \\
\text{where } \Gamma_i(\mathbf{R}) &= \left\{ z \in C : |z - r_0| \leq \max_{i\in N} a_i(\mathbf{R}) \right\} \\
a_i(\mathbf{R}) &= \sum_{i\neq j} |r_{ij}| \\
\left\lceil \frac{n}{2} \right\rceil &= \begin{cases} \dfrac{n}{2}, & \text{if } n \text{ is even,} \\ \dfrac{n+1}{2}, & \text{if } n \text{ is odd.} \end{cases}
\end{aligned} \tag{12}$$

$\Gamma(\mathbf{R})$ is the union of the Gershgorin set of discs for the covariance matrix $\mathbf{R}$. Although the Gershgorin disc theorem provides a good inclusion bound for the eigenvalues, the Brauer disc theorem provides a tighter inclusion bound that depends on the row and column summations for the region of the eigenvalues.

Theorem 2 (Brauer Disc Theorem [17]): Let $\mathbf{R} = [r_{ij}] \in \mathbb{C}^{n\times n}$ be a Toeplitz matrix, $r_{ii} = r_0, n \geqslant 2$ and $\sigma(\mathbf{R})$ be spectrum of $\mathbf{R}$. Then,

$$\begin{aligned}
\sigma(\mathbf{R}) \subseteq \Upsilon(\mathbf{R}) &= \bigcup_{i=1}^{\lceil \frac{n}{2} \rceil} \Upsilon_i(\mathbf{R}) \\
\text{where } \Upsilon_i(\mathbf{R}) &= \{ z \in C : |z - r_0| \leq D \} \\
D &= \max_{i,j\in N, i\neq j} \sqrt{a_i(\mathbf{R}) a_j(\mathbf{R})} \\
a_i(\mathbf{R}) &= \sum_{i\neq j} |r_{ij}| \\
\left\lceil \frac{n}{2} \right\rceil &= \begin{cases} \dfrac{n}{2}, & \text{if } n \text{ is even,} \\ \dfrac{n+1}{2}, & \text{if } n \text{ is odd.} \end{cases}
\end{aligned} \tag{13}$$

where $\Upsilon(\mathbf{R})$ is the union of the Brauer disc set of covariance matrix $\mathbf{R}$. Based on [18], the Brauer eigenvalue inclusion set is tighter than the Gershgorin set such that $\Upsilon(\mathbf{R}) \subseteq \Gamma(\mathbf{R})$. An example is shown in Fig. 3. In addition, the maximum eigenvalue of $\mathbf{R}$ is associated with the largest Gershgorin and Brauer discs [37]. The BD theorem will be used to establish a cluster bound around clutter-plus-noise THPD covariance matrices.

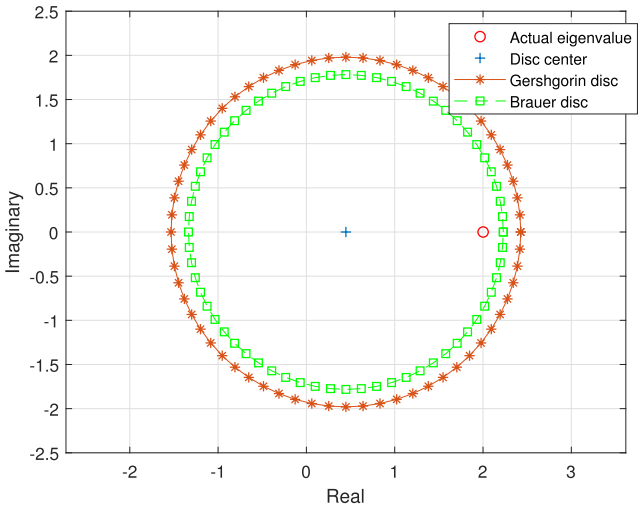

FIGURE 3. Example of a Gershgorin and Brauer disc for the maximum eigenvalue of a covariance matrix R.

V. APPLICATION TO RADAR DETECTION

In this section, two non-parametric CFAR detectors based on Riemannian and Euclidean spaces are presented. The constraint for both CFAR detectors uses Gaussian approximation of the underlying distribution, so that the covariance matrix estimation can be used with our proposed CFAR detectors. Also, the minimum number of snapshots required is equal to the number of antenna elements to be able to have a successful detection.

Consider M snapshots received by an antenna array of N elements, $\mathbf{x}^i = (x_0, \ldots, x_{N-1})$ for $i = 1, 2, \ldots, M$. Stage one of the proposed CFAR detectors exploits RBA, which converts each snapshot to a THPD covariance matrix and establishes a clutter-plus-noise cluster bound and potential targets bound around the maximum eigenvalues of the THPD covariance matrices using the BD theorem. The RBM-CFAR detector is based on the Riemannian distance between the Riemannian mean of the clutter-plus-noise THPD covariance matrices and the potential target THPD covariance matrices on the Riemannian manifold. The ABHB-CFAR detector takes advantage of the law of cosines on the Riemannian manifold to compute the detection angle between the Riemannian mean, the Riemannian median and the potential target points residing on the Riemannian manifold.

A. RD-CFAR DETECTOR

Arnaudon *et al.,* [20] developed a new matrix CFAR detector based on the Riemannian space of Hermitian positive definite matrices (HPD) that outperforms the FFT-CFAR detector. Unlike the classical CFAR detectors where the range bins are used to compute a single maximum likelihood sample covariance matrix [38], the RD-CFAR detector converts every range bin into an HPD covariance matrix and computes the Riemannian mean of the reference HPD covariance matrices excluding the guard THPD covariance matrices as illustrated

in Fig. 4. Specifically, RD-CFAR is based on the Riemannian distance d_R between the Riemannian mean $\mathbf{R}_{rm}$ of the reference HPD covariance matrices and the HPD matrix under test $\mathbf{R_D}$. The Riemannian distance is compared with the adaptive detection threshold T calculated using the clutter power level (trace of the $\mathbf{R}_{rm}$) and the desired probability of false alarm.

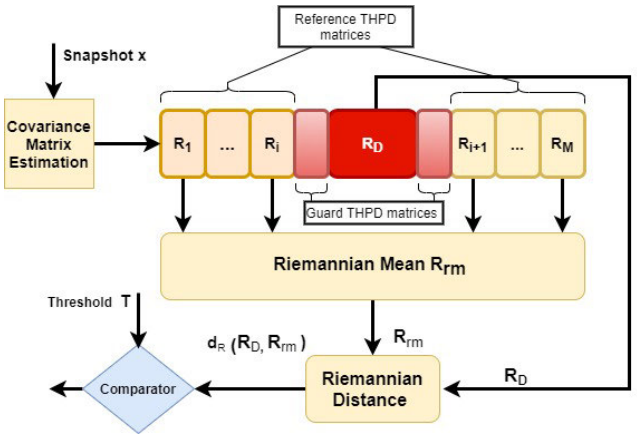

FIGURE 4. RD-CFAR detector.

The RD-CFAR detector is based on the Riemannian distance, which can be written as

$$d_R(\mathbf{R}_D, \mathbf{R}_{rm}) \underset{H_0}{\overset{H_1}{\gtrless}} \mathrm{T}. \tag{14}$$

The RD-CFAR detector outperforms the cell FFT-CFAR detector based on spectral estimation [24]. However, the computational cost of RD-CFAR is high since the number of Riemannian mean computations is equal to the number of snapshots M. The RD-CFAR detection process is shown in Fig. 4.

B. BRAUER CLUSTER BOUND

The BD theorem can be exploited to establish a cluster bound around the maximum eigenvalues of the THPD covariance matrices. The maximum eigenvalues of THPD covariance matrices are associated with the largest BD. The centre of the largest BD, which is the inclusion region for the maximum eigenvalue, represents the power of the snapshot P_0 as shown in Algorithm 1. In addition, the minimum BD radius ρ of the maximum eigenvalues of the THPD covariance matrices represents the minimum bound of the clutter-plus-noise. Using the BD centres of all THPD covariance matrices c_i, the Brauer cluster bound T_B for the clutter-plus-noise can be established as

$$T_B = \frac{\frac{1}{M}\sum_{i=1}^{M} c_i}{\left(\prod_{i=1}^{M} c_i\right)^{\frac{1}{M}}}\rho \tag{15}$$

where $\frac{1}{M}\sum_{i=1}^{M} c_i$ and $\left(\prod_{i=1}^{M} c_i\right)^{\frac{1}{M}}$ are the arithmetic mean and geometric mean of the centres of the Brauer discs, respectively. The THPD covariance matrices corresponding to the eigenvalues inside the Brauer cluster bound are considered clutter-plus-noise covariance matrices. On the other hand, the THPD covariance matrices associated with the eigenvalues outside the Brauer cluster bound are considered THPD matrices of potential targets. An example of a Brauer cluster bound with the BD theorem for maximum eigenvalues of the THPD covariance matrices is shown in Fig. 5. As can be seen in Fig. 5, all eigenvalues are inside the Brauer cluster bound except two that can be considered potential targets.

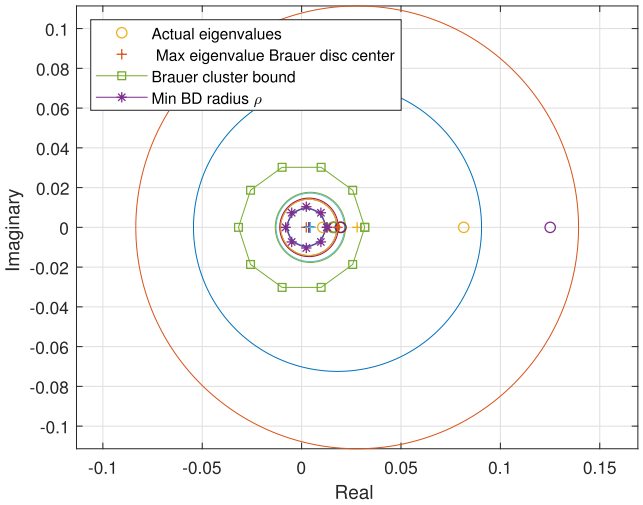

FIGURE 5. Example of Brauer cluster bound for clutter-plus-noise eigenvalues.

C. RIEMANNIAN-BRAUER MATRIX CFAR DETECTOR

The RBM-CFAR detector is a two stage process based on the Riemannian distance between Riemannian mean and the THPD covariance matrices of potential targets. The first stage uses the RBA to convert each range cell into a THPD covariance matrix and exploits the BD theorem to cluster the maximum eigenvalues of the THPD covariance matrices. By using (15), a clutter-plus-noise cluster bound and potential target bound of the THPD covariance matrices can be established. The second stage involves computing the Riemannian distance d_{RB} between the Riemannian mean of the clutter-plus-noise THPD covariance matrices and the potential target THPD covariance matrices. The rule of detection for the RBM-CFAR detector can be formulated using (7), (9) and (15) as

$$d_{RB}(\mathbf{R}_{rm}(T_B), \mathbf{R}_{T_i}) \underset{H_0}{\overset{H_1}{\gtrless}} \delta \tag{16}$$

where $\mathbf{R}_{rm}(T_B)$ is the Riemannian mean of the THPD covariance matrix inside the Brauer cluster bound, $\mathbf{R}_{T_i}$ is the THPD covariance matrix of a potential target and δ is an adaptive threshold. δ is based on the probability of false alarm P_{fa} and clutter power levels and is given by

$$\delta = -\mathrm{tr}(\mathbf{R}_{rm})\ln(P_{fa}). \tag{17}$$

The RBM-CFAR detector, as illustrated in Fig. 6, has many advantages over RD-CFAR in [20]. First, the Riemannian mean and median are robust to outliers since THPD covariance matrices of all potential targets are not included in the computation process. Second, the computational cost is less since the Riemannian mean is only calculated once in Fig. 6 as opposed for each snapshot in RD-CFAR as shown in Fig. 4. Also, the Riemannian distance calculation depends on the number of outliers as shown in Fig. 6.

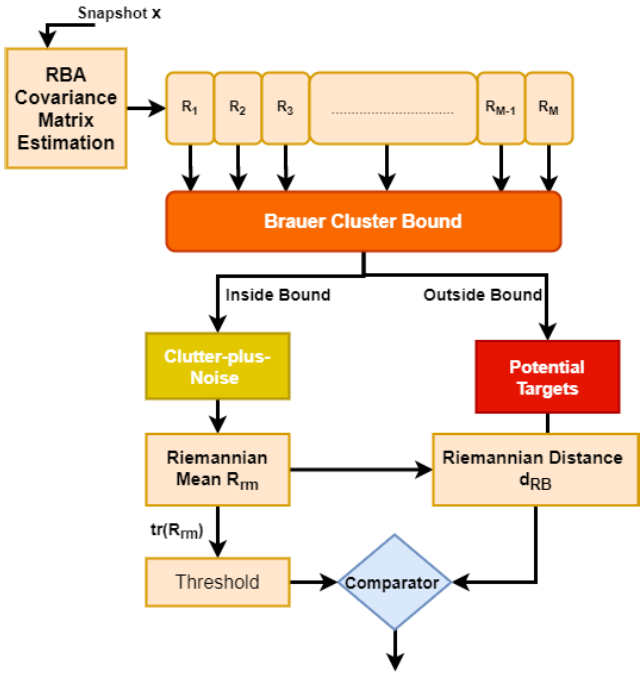

FIGURE 6. RBM-CFAR detector.

D. ANGLE-BASED HYBRID-BRAUER CFAR DETECTOR

The ABHB-CFAR detector makes use of the RBA to convert the range cells to THPD covariance matrices and establishes a Brauer cluster bound around the maximum eigenvalues of the THPD covariance matrices. By using (15), a clutter-plus-noise cluster bound and the potential target bound of the THPD covariance matrices is created. The ABHB-CFAR detector exploits the Euclidean tangent space and the Riemannian geodesical distances between points on the Riemannian manifold. Also, the ABHB-CFAR uses the projection of both the Riemannian mean and median onto the tangent space of the potential target point. A geodesical triangle connecting the projected Riemannian mean, the projected Riemannian median and the potential target can be generated and the law of cosines can be used [39] to compute the Riemannian angle at the potential target as shown in Fig. 7.

If $\{a, b, c\}$ lie in the Euclidean space, the law of cosines states that

$$\|b-c\|^2 = \|\text{b-a}\|^2 + \|\text{c-a}\|^2 - 2\langle b-a, \text{c-a}\rangle \tag{18}$$

where $\|\cdot\|$ is the ℓ_2-norm and $\langle , \rangle$ represents the dot product. The law of cosines can be applied to the geodesic triangle on the Riemannian manifold where the vertices of the triangle are the Riemannian mean $\mathbf{R}_{rm}$, the Riemannian median $\mathbf{R}_{rmed}$ and the potential target point $\mathbf{R}_{T_i}$, using (7), (8), (9), (10), (15) and (18) to give

$$\begin{aligned}\|d_R(\mathbf{R}_{rm}, \mathbf{R}_{rmed})\|^2 = &\left\|d_R(\mathbf{R}_{rm}, \mathbf{R}_{T_i})\right\|^2 \\ &+ \left\|d_R(\mathbf{R}_{rmed}, \mathbf{R}_{T_i})\right\|^2 \\ &- 2\left\langle \text{logm}_{\mathbf{R}_{T_i}}(\mathbf{R}_{rm}), \text{logm}_{\mathbf{R}_{T_i}}(\mathbf{R}_{rmed})\right\rangle\end{aligned} \tag{19}$$

where $\text{logm}_{\mathbf{R}_{T_i}}(\mathbf{R}_{rm})$ is the projection of $\mathbf{R}_{rm}$ onto the tangent space of $\mathbf{R}_{T_i}$. The dot product term can be written in terms of angle as

$$\begin{aligned}&\left\langle \text{logm}_{\mathbf{R}_{T_i}}(\mathbf{R}_{rm}), \text{logm}_{\mathbf{R}_{T_i}}(\mathbf{R}_{rmed})\right\rangle \\ &\quad = \left\|\text{logm}_{\mathbf{R}_{T_i}}(\mathbf{R}_{rm})\right\| \left\|\text{logm}_{\mathbf{R}_{T_i}}(\mathbf{R}_{rmed})\right\| \cos(\theta)\end{aligned} \tag{20}$$

where θ is the angle at point $\mathbf{R}_{T_i}$ on the tangent space, which can be written as

The rule of detection for the ABHB-CFAR detector can be formulated using (21), shown at the bottom of the page

$$\theta \underset{H_1}{\overset{H_0}{\gtrless}} \gamma \tag{22}$$

where γ is the adaptive angle of detection, which can be formulated using (17), (19) and median-based threshold as in (23), shown at the bottom of the page.

The farther the potential target, the smaller the angle on the manifold. The ABHB-CFAR detector is illustrated in Fig. 8.

$$\cos(\theta) = \frac{\left\|d_R(\mathbf{R}_{rm}, \mathbf{R}_{T_i})\right\|^2 + \left\|d_R(\mathbf{R}_{rmed}, \mathbf{R}_{T_i})\right\|^2 - \|d_R(\mathbf{R}_{rm}, \mathbf{R}_{rmed})\|^2}{2\left\|\text{logm}_{\mathbf{R}_{T_i}}(\mathbf{R}_{rm})\right\| \left\|\text{logm}_{\mathbf{R}_{T_i}}(\mathbf{R}_{rmed})\right\|} \tag{21}$$

$$\gamma = \text{acos}\left(\frac{\left\|-\text{tr}(\mathbf{R}_{rm})\ln(P_{fa})\right\|^2 + \left\|\text{tr}(\mathbf{R}_{rmed})\ln(P_{fa})\right\|^2 - \|d_R(\mathbf{R}_{rm}, \mathbf{R}_{rmed})\|^2}{2\left\|-\text{tr}(\mathbf{R}_{rm})\ln(P_{fa})\right\| \left\|\text{tr}(\mathbf{R}_{rmed})\ln(P_{fa})\right\|}\right) \tag{23}$$

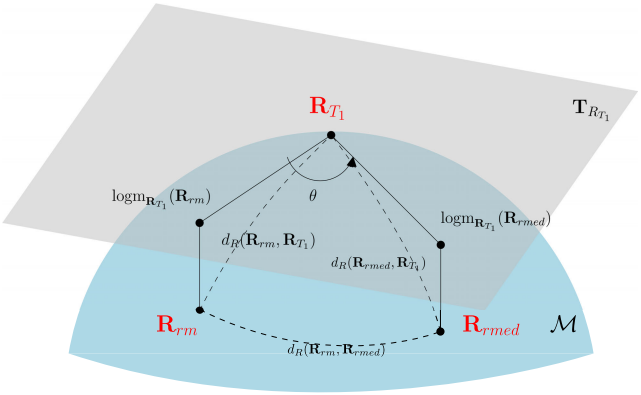

FIGURE 7. Geodesical triangle showing the angle at potential target on the manifold.

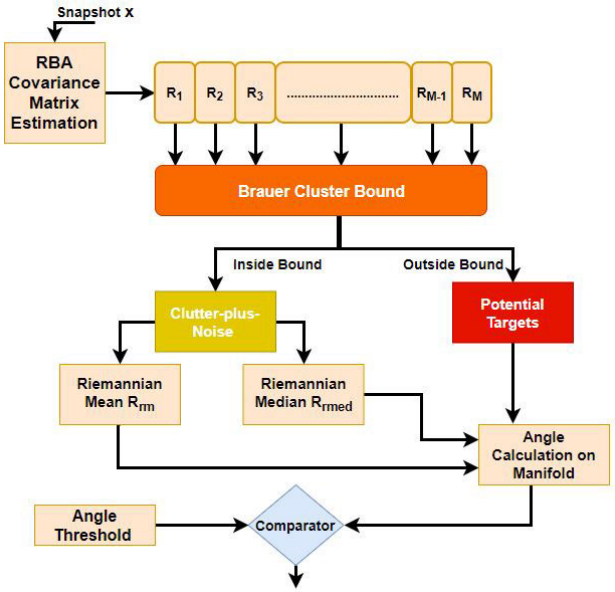

FIGURE 8. ABHB-CFAR detector.

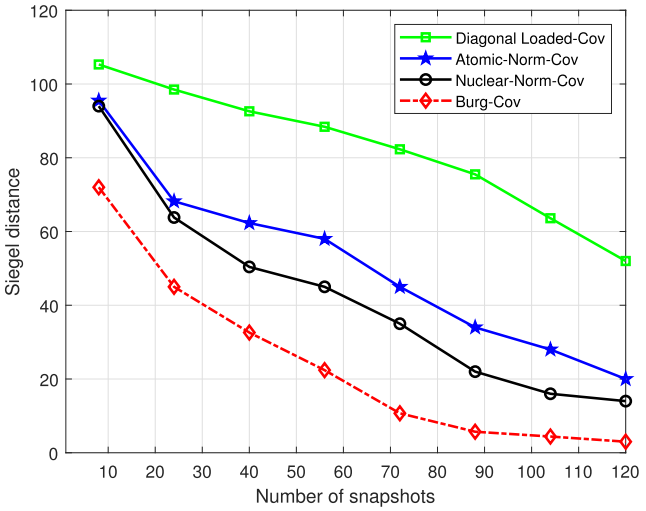

FIGURE 9. Siegel distance between the asymptotic covariance matrix and the estimated THPD covariance matrices from the RBA, the atomic-norm minimization, the nuclear norm minimization and the diagonally loaded sample covariance.

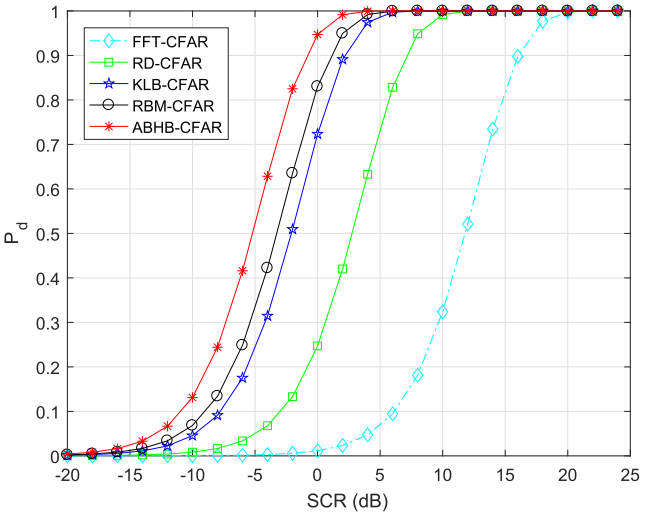

FIGURE 10. Performance comparison of the FFT-CFAR, the RD-CFAR, the KLB-CFAR, RBM and the ABHB CFAR at $P_{fa} = 10^{-3}$.

VI. SIMULATIONS AND RESULTS

The simulations in this section consist of two parts: measuring the Siegel distance [40] between the asymptotic covariance matrix and the estimated THPD covariance matrices from RBA, atomic-norm minimization [12], nuclear norm minimization [13] and diagonal loading and evaluating the performance of the FFT-CFAR, the RD-CFAR, the KLB-CFAR, the RBM and the ABHB CFAR detectors. The RBA regularization parameter, ψ_1, is set to 0.1 and the autoregressive order model is set to 8, which is equal the number of receivers in the antenna array. Also, the Riemannian mean step size, ϵ, is set to 0.01 and the number of iterations, t, is set to 10000 with convergence tolerance level set to 10^{-6}. A collocated uniform linear array is used with $N = 8$ receivers and the antenna elements are spaced half a wavelength apart from each other.

The first part of the simulations is based on measuring the Siegel distance [40], which is the geodesical distance between two covariance matrices in the space of HPD matrices. The data is generated from one received pulse with different number of snapshots. For different number of snapshots, the THPD covariance matrices are estimated using the RBA, the atomic-norm minimization, the nuclear norm minimization and the diagonally loaded sample covariance. The main idea is to measure the Siegel distance between the asymptotic covariance matrix and the estimated THPD covariance matrices, where ideally the Siegel distance would be zero. For the simulations results shown in Fig. 9, the THPD covariance matrices are estimated using RBA, atomic-norm minimization, nuclear norm minimization and diagonal loading across increasing number of snapshots. We notice that the rate of convergence of RBA is faster than the other techniques as the number of snapshots increases. Also, the atomic-norm

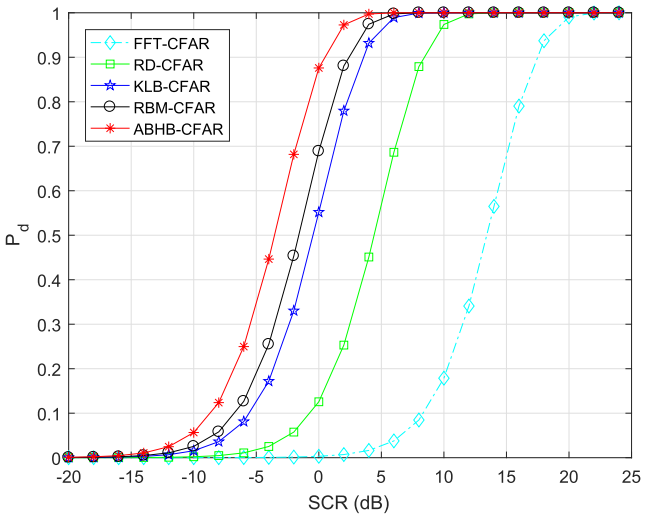

FIGURE 11. Performance comparison of the FFT-CFAR, the RD-CFAR, the KLB-CFAR, the RBM and the ABHB CFAR at $P_{fa} = 10^{-4}$.

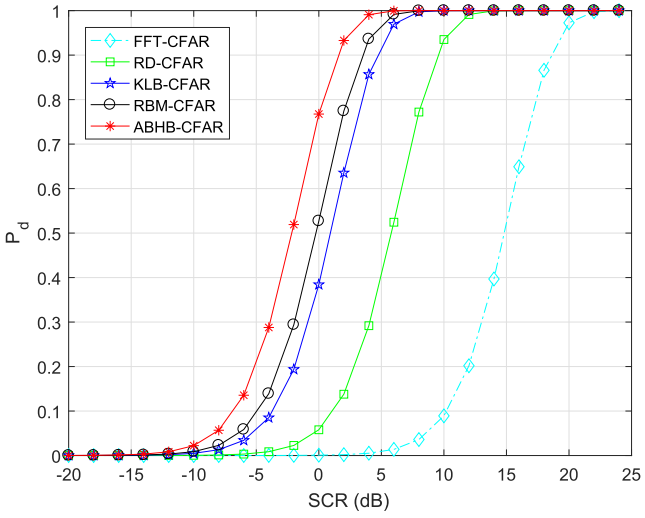

FIGURE 12. Performance comparison of the FFT-CFAR, the RD-CFAR, the KLB-CFAR, the RBM and the ABHB CFAR at $P_{fa} = 10^{-5}$.

minimization and the nuclear-norm minimization outperformed the diagonally loaded sample covariance. This indicates that the RBA-based covariance matrix, which is the mean of the estimated THPD covariance matrices from each snapshot (range bin), converges to the asymptotic covariance matrix with fewer snapshots in comparison with the other techniques.

The second part of the simulation results are presented to evaluate the performance of the RBM-CFAR and the ABHB-CFAR techniques in comparison with the FFT-CFAR, the RD-CFAR and the KLB-CFAR detectors via Monte Carlo simulations. The data is generated from 5 received pulses and $M = 25$ snapshots with a target moving with a velocity $v = 10\ m/s$ travelling away from the radar at a range of 50 m. The target is located at the 10^{th} snapshot. The clutter model is based on a Weibull distribution with scale parameter $\alpha = 1$

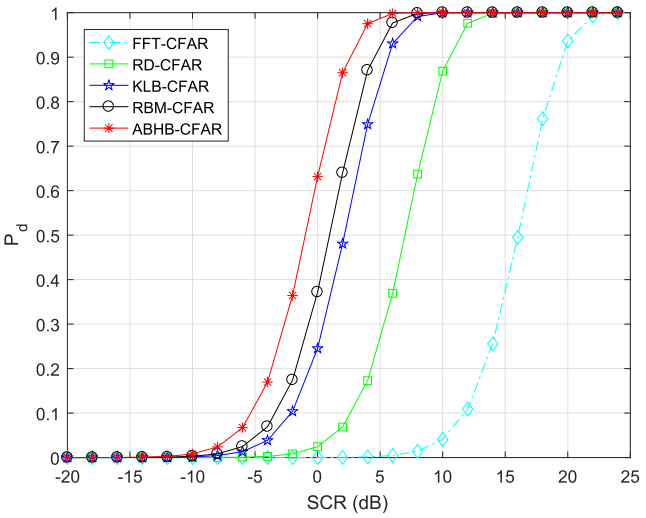

FIGURE 13. Performance comparison of the FFT-CFAR, the RD-CFAR, the KLB-CFAR, the RBM and the ABHB CFAR at $P_{fa} = 10^{-6}$.

and shape parameter $\beta = 3$. The covariance matrix model Σ_d for generating the snapshots can be defined as [29]

$$\Sigma_d(i,k) = \sigma_c^2 \rho^{|i-k|} \exp(j2\pi \frac{v}{\lambda}(i-k)) \quad i,k = 1,\ldots,N \tag{24}$$

where σ_c is the clutter power, ρ is the one lag correlation coefficient and λ is the wavelength. In this simulation, we set $\rho = 0.9$ and $\lambda = 1$ m.

For the FFT-CFAR, 10 cells are used for averaging and for the RD-CFAR and the KLB-CFAR, 10 THPD covariance matrices are used for averaging. The RBM-CFAR and ABHB-CFAR Riemannian mean is based on the THPD covariance matrix snapshots inside the BD cluster bound, which does not include any potential targets and is not biased to any outlier. The covariance matrix model for

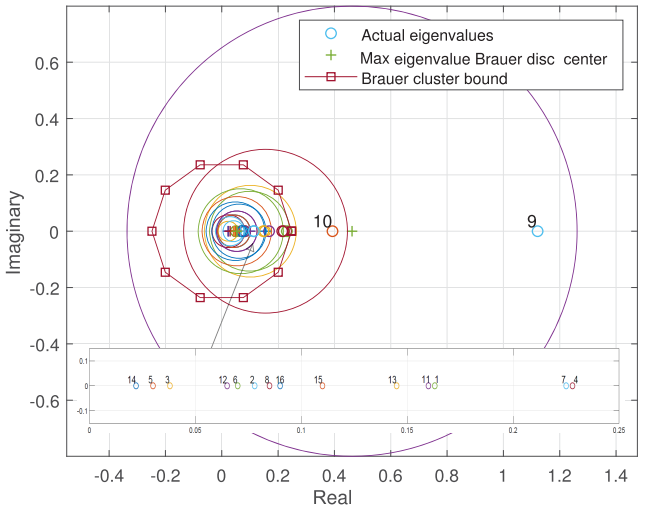

FIGURE 14. Brauer bound for clutter-plus-noise and potential targets at the 9^{th} and 10^{th} range bins for pulse 1.

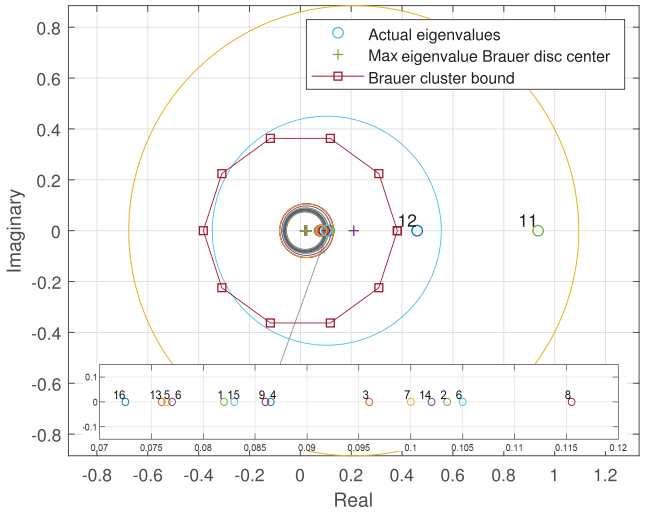

FIGURE 15. Brauer bound for clutter-plus-noise and potential targets at the 11^{th} and 12^{th} range bins for pulse 2.

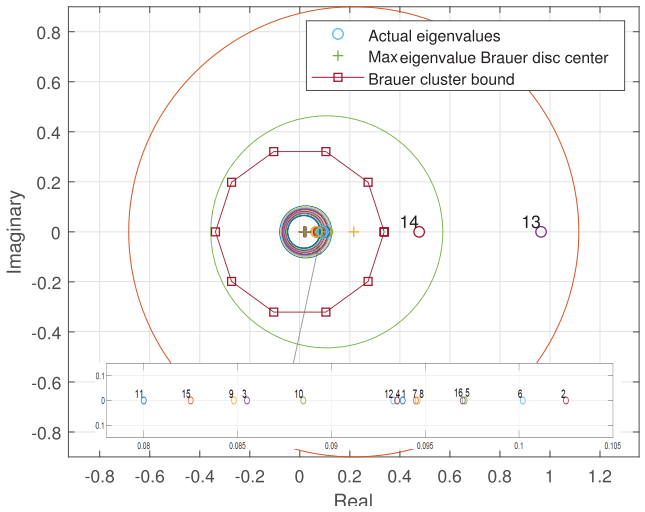

FIGURE 16. Brauer bound for clutter-plus-noise and potential targets at the 13^{th} and 14^{th} range bins for pulse 3.

the RD-CFAR, the KLB-CFAR, the RBM-CFAR and the ABHB-CFAR is based on (3).

The detection threshold calculation depends on the clutter background power, the threshold multiplier and the probability of false alarm P_{fa}. The threshold multiplier can be computed using P_{fa}, number of average snapshots or cells, and the shape parameter β of the Weibull distribution clutter model [41]. The Monte Carlo simulation is based on 200, 000 runs to determine the probability of detection P_d and the threshold levels. The performance of all the five detectors for different P_{fa} are shown in Figs. 10 to 13. The simulation results demonstrate that both the RD-CFAR and the KLB-CFAR outperform the FFT-CFAR. Also, the performance of the RBM-CFAR and the ABHB-CFAR is better than the RD-CFAR and the KLB-CFAR with at least 2–5 dB signal-to-clutter improvement.

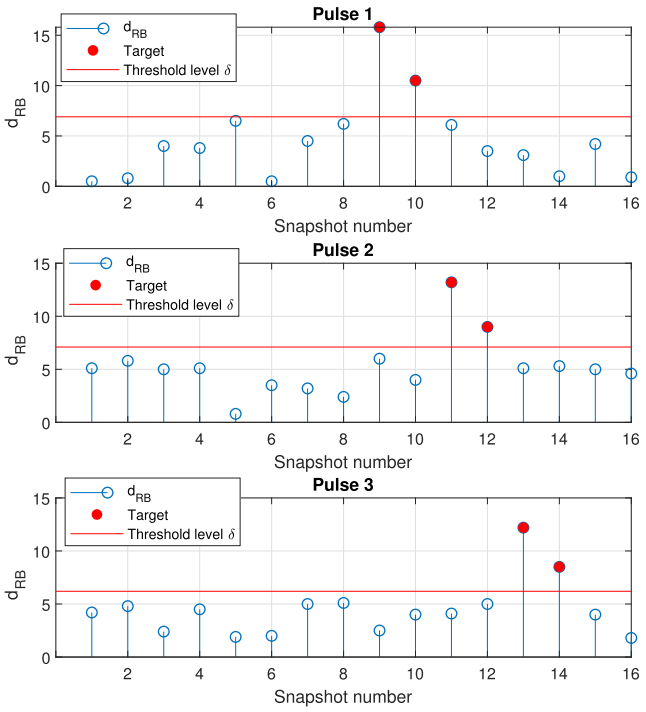

FIGURE 17. Detection performance of the RBM-CFAR detector for three consecutive pulses with a moving target.

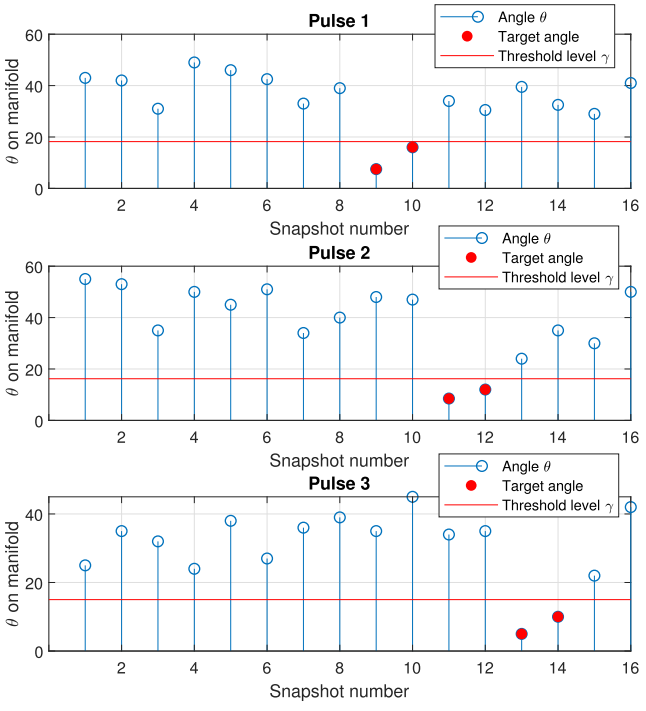

FIGURE 18. Detection performance of the ABHB-CFAR detector for three consecutive pulses with a moving target.

VII. REAL DATA ANALYSIS

The performance of the RBM and the ABHB CFAR detectors were tested using real data from a drone detection experiment. The data was collected using a Texas

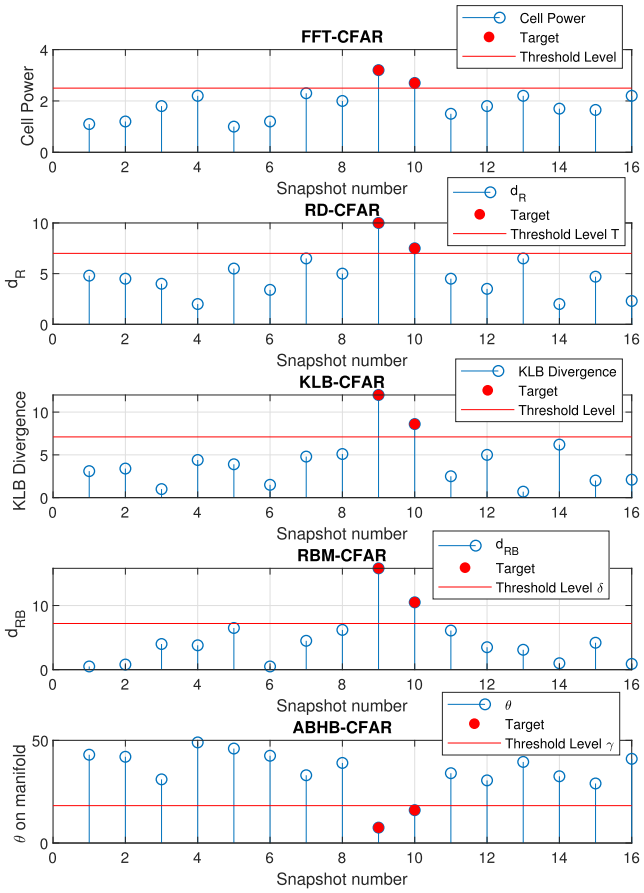

FIGURE 19. Detection performance of the FFT-CFAR, the RD-CFAR, the KLB-CFAR, the RBM-CFAR and the ABHB-CFAR detectors for pulse 1.

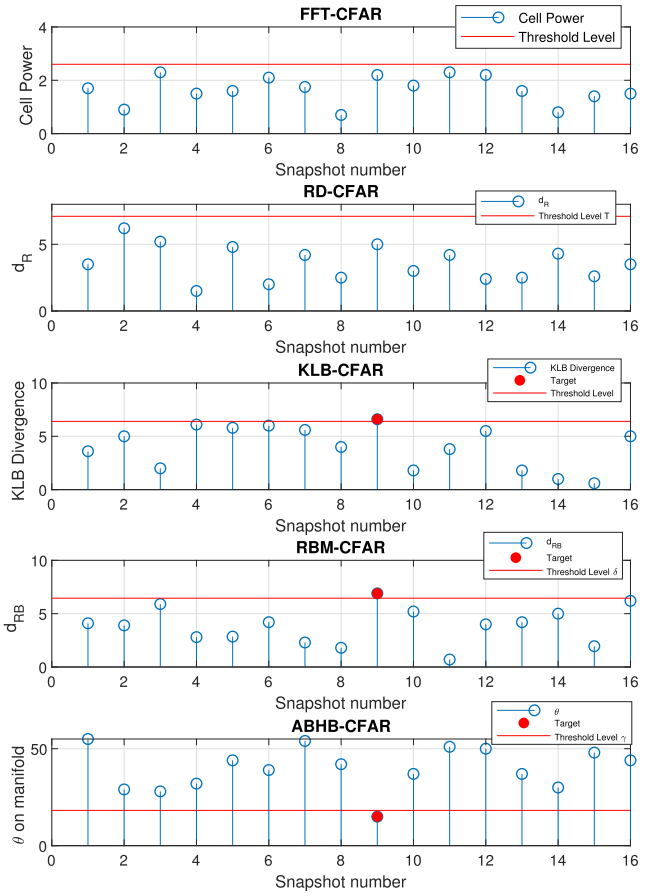

FIGURE 20. Detection performance of the FFT-CFAR, the RD-CFAR, the KLB-CFAR, the RBM-CFAR and the ABHB-CFAR detectors under scaled SNR for pulse 1.

Instruments AWR1642 automotive radar with a moving Yuneec Typhoon H drone target at 5 m range travelling away from the radar. The AWR1642 radar is based on frequency-modulated continuous-wave (FMCW) with integrated phase locked loop and analog-to-digital converter. The experiment parameters and the radar specifications are given in Table 1.

TABLE 1. AWR1642 automotive radar specifications.

Feature	Specification
Centre freq.	76–81 GHz
Bandwidth	4 GHz
Pulse Repetition Frequency	26.3 KHz
Receive Channels	4 Antennas
Transmit Channels	2 Antennas
Transmit Power	12.5 dBm
Range Resolution	3.75 cm
Elevation Angle	15 degrees
Azimuth Angle	0 degrees
Max Range	45 metres
Antenna Gain	30 dB

The performance of the proposed techniques is tested for 3 consecutive pulses with 16 range cells (snapshots) extracted from the data set. The extracted snapshots are converted to THPD covariance matrices using the RBA and a clutter-plus-noise bound established using BD theorem. As we can see from Figs. 14 to 16, there are some points outside the clutter-plus-noise bound and they are considered as potential targets. The detection threshold calculation is based on $P_{fa} = 10^{-3}$. In addition, Figs. 17 and 18 show the RBM-CFAR and the ABHB-CFAR detection for three consecutive pulses that exhibit some robustness in their performance. For the RBM detector, the Riemannian distance of both the 9^{th} and 10^{th} snapshots of the first pulse exceeded the detection threshold. Likewise, for the ABHB detector the 9^{th} and 10^{th} snapshots of the first pulse also have minimum angles. However, the AWR1642 data set contains only one target and the detection techniques are showing potentially two targets due to the range resolution of the AWR1642 being 3.75 cm and the target occupying two range bins (two snapshots). The 9^{th} snapshot contains most of the target's energy and the 10^{th} contains some of the target's energy. Furthermore, similar performance for pulses 2 and 3 are shown in Figs. 17 and 18.

The performance of the RBM-CFAR and the ABHB-CFAR techniques is compared with the FFT-CFAR, the RD-CFAR and the KLB-CFAR in Fig. 19. We notice that all techniques detected the target at range bins 9 and 10 since

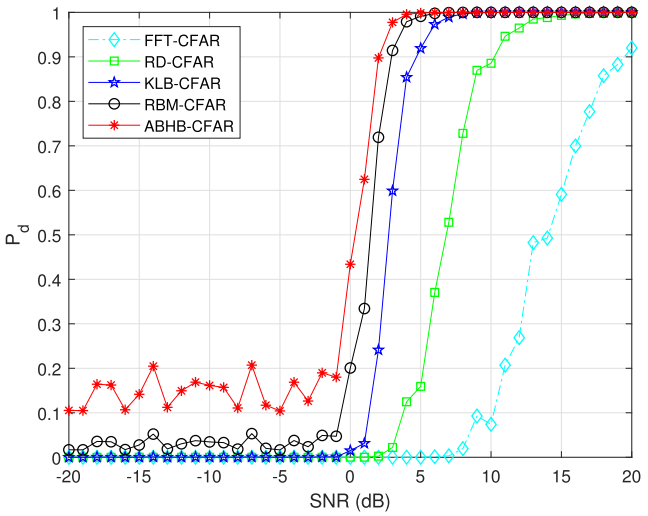

FIGURE 21. Operating characteristic curves for the FFT-CFAR, the RD-CFAR, the KLB-CFAR, the RBM-CFAR and the ABHB-CFAR detectors at $P_{fa} = 10^{-4}$.

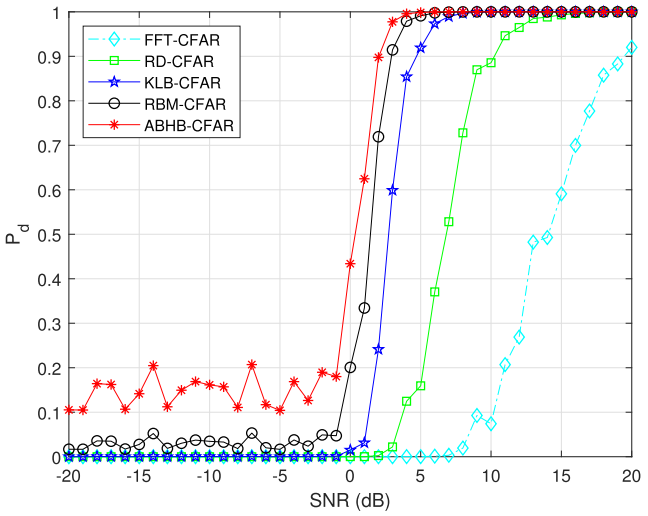

FIGURE 22. Operating characteristic curves for the FFT-CFAR, the RD-CFAR, the KLB-CFAR, the RBM-CFAR and the ABHB-CFAR detectors at $P_{fa} = 10^{-5}$.

the data collected has high SNR. By scaling the SNR by 0.2, the performance of the FFT-CFAR and the RD-CFAR degraded in comparison to the KLB-CFAR, the RBM-CFAR and the ABHB-CFAR as shown in Fig. 20. In addition, the ABHB-CFAR and the RBM-CFAR outperformed the KLB-CFAR and maintained the largest Riemannian distance and the smallest angle on the Riemannian manifold target point. Furthermore, the performance of the proposed CFAR detectors can be studied by varying the SNR of the real data and maintaining a constant P_{fa}. Figures 21 and 22 illustrate the detection performance at $P_{fa} = 10^{-4}$ and 10^{-5}. At higher SNR, all the CFAR detectors maintain a good detection performance. However, at lower SNR (less than 5 dB) and $P_{fa} = 10^{-4}$, both the FFT-CFAR and the RD-CFAR detectors suffer degradation in performance in comparison with the other CFARs due to the limited number of range cells. Also, at $P_{fa} = 10^{-5}$ the RBM-CFAR and the ABHB-CFAR showed superior performance while the KLB-CFAR, the FFT-CFAR and the RD-CFAR failed to retain their detection performances.

VIII. CONCLUSION

The drone detection problem is viewed from a Riemannian geometry perspective. Two novel CFAR detection techniques, the RBM and the ABHB, were formulated to improve the probability of detection under small sample size with low SCR. The RBM-CFAR and the ABHB-CFAR showed an improvement in the probability of detection in comparison with the FFT-CFAR, the RD-CFAR and the KLB-CFAR. In addition, the BD theorem provided robustness to the calculation of the Riemannian mean and median by excluding outliers from the Riemannian mean and median computations. Real data analysis showed that the proposed CFAR detectors can achieve better performance for low SNR, low sample size data and high probability of false alarm. In addition, the ABHB-CFAR showed a better performance in comparison with the RBM-CFAR under low SNR. These results are based on a uniform linear array configuration. Future work will study the sub-optimality of other array configurations. Furthermore, future research will investigate different geometric divergence measures in computing the geometric mean and median and its effect on the detection process.

REFERENCES

[1] N. Amrouche, A. Khenchaf, and D. Berkani, "Tracking and detecting moving weak targets," *Adv. Sci., Technol. Eng. Syst. J.*, vol. 3, no. 1, pp. 467–471, Jan. 2018.

[2] T. Shan, S. Liu, R. Tao, and G. Zhang, "Experiment demonstration of micro-Doppler detection of rotor blades with passive coherent location based on digital video broadcast," *J. Commun. Technol. Electron.*, vol. 59, no. 11, pp. 1215–1224, 2014.

[3] A. Digulescu, C. Despina-Stoian, D. Stănescu, F. Popescu, F. Enache, C. Ioana, E. Rădoi, I. Rîncu, and A. Şerbănescu, "New approach of UAV movement detection and characterization using advanced signal processing methods based on UWB sensing," *Sensors*, vol. 20, no. 20, pp. 5904–5922, Oct. 2020. [Online]. Available: https://www.mdpi.com/1424-8220/20/20/5904

[4] M. Richards, *Fundamentals of Radar Signal Processing*, 2nd ed. New York, NY, USA: McGraw-Hill, 2014.

[5] S. Amari, "Information geometry on hierarchy of probability distributions," *IEEE Trans. Inf. Theory*, vol. 47, no. 5, pp. 1701–1711, Jul. 2001.

[6] S. Amari and T. S. Han, "Statistical inference under multiterminal rate restrictions: A differential geometric approach," *IEEE Trans. Inf. Theory*, vol. 35, no. 2, pp. 217–227, Mar. 1989.

[7] R. Bhatia and J. Holbrook, *Riemannian Geometry and Matrix Geometric Mean, Linear Algebra and its Applications*. Amsterdam, The Netherlands: Elsevier, 2006.

[8] S. Lang, *Fundamentals of Differential Geometry*. New York, NY, USA: Springer, 1999.

[9] K. M. Wong, J.-K. Zhang, J. Liang, and H. Jiang, "Mean and median of PSD matrices on a Riemannian manifold: Application to detection of narrow-band sonar signals," *IEEE Trans. Signal Process.*, vol. 65, no. 24, pp. 6536–6550, Dec. 2017.

[10] M. Arnaudon, F. Barbaresco, and L. Yang, *Medians and Means in Riemannian Geometry: Existence Uniqueness and Computation Matrix Information Geometry*. New York, NY, USA: Springer, 2012.

[11] J. Burg, "Maximum entropy spectral analaysis," Ph.D. dissertation, Dept. Geophys., Stanford Univ., Stanford, CA, USA, 1975.
[12] X. Wu, W.-P. Zhu, and J. Yan, "A Toeplitz covariance matrix reconstruction approach for direction-of-arrival estimation," *IEEE Trans. Veh. Technol.*, vol. 66, no. 9, pp. 8223–8237, Sep. 2017.
[13] W. Tan and X. Feng, "Covariance matrix reconstruction for direction finding with nested arrays using iterative reweighted nuclear norm minimization," *Int. J. Antennas Propag.*, vol. 2019, pp. 1–13, Mar. 2019.
[14] H. Chung, J. Joo, and S. Kim, "Off-grid DoA estimation on non-uniform linear array using constrained Hermitian matrix," *Energies*, vol. 13, no. 21, p. 5775, Nov. 2020.
[15] R. S. Varga, *Gersgorin and His Circles*. Berlin, Germany: Springer, 2004.
[16] C. Sang and J. Zhao, "Eventually DSDD matrices and eigenvalue localization," *Symmetry*, vol. 10, no. 10, p. 448, Oct. 2018.
[17] C. Li and Y. Li, "New regions including eigenvalues of Toeplitz matrices," *Linear Multilinear Algebra*, vol. 62, no. 2, pp. 229–241, Feb. 2014.
[18] A. Melman, "Modified Gershgorin disks for companion matrices," *SIAM Rev.*, vol. 54, no. 2, pp. 355–373, Jan. 2012.
[19] R. E. Kass and P. W. Vos, *Geometrical Foundations of Asymptotic Inference*. Hoboken, NJ, USA: Wiley, 2011.
[20] M. Arnaudon, F. Barbaresco, and L. Yang, "Riemannian medians and means with applications to radar signal processing," *IEEE J. Sel. Topics Signal Process.*, vol. 7, no. 4, pp. 595–604, Aug. 2013.
[21] F. Barbaresco, "Information geometry manifold of Toeplitz Hermitian positive definite covariance matrices: Mostow/Berger fibration and Berezin quantization of Cartan-Siegel domains," *Int. J. Emerg. Trends Signal Process.*, vol. 1, no. 3, pp. 1–87, Mar. 2013.
[22] F. Barbaresco, "Super-resolution spectrum analysis regularization: Burg, Capon & AGO-antagonistic algorithms," in *Proc. 8th Eur. Signal Process. Conf. (EUSIPCO)*, Sep. 1996, pp. 1–4.
[23] J. Lapuyade-Lahorgue and F. Barbaresco, "Radar detection using siegel distance between autoregressive processes, application to HF and X-band radar," in *Proc. IEEE Radar Conf.*, May 2008, pp. 1–6.
[24] Z. Yang, Y. Cheng, and H. Wu, "PCA-based matrix CFAR detection for radar target," *Entropy*, vol. 22, no. 7, p. 756, Jul. 2020.
[25] X. Hua, Y. Cheng, H. Wang, Y. Qin, Y. Li, and W. Zhang, "Matrix CFAR detectors based on symmetrized Kullback–Leibler and total Kullback–Leibler divergences," *Digit. Signal Process.*, vol. 69, pp. 106–116, Oct. 2017.
[26] Y. Cheng, X. Hua, H. Wang, Y. Qin, and X. Li, "The geometry of signal detection with applications to radar signal processing," *Entropy*, vol. 18, no. 11, p. 381, Oct. 2016.
[27] F. D. A. García, A. C. F. Rodriguez, G. Fraidenraich, and J. Filho, "CA-CFAR detection performance in homogeneous Weibull clutter," *IEEE Geosci. Remote Sens. Lett.*, vol. 16, no. 6, pp. 887–891, Jun. 2019.
[28] D. C. Schleher, "Radar detection in Weibull clutter," *IEEE Trans. Aerosp. Electron. Syst.*, vol. AES-12, no. 6, pp. 736–743, Nov. 1976.
[29] R. Vicen-Bueno, M. Rosa-Zurera, L. Cuadra-Rodriguez, and D. De La Mata-Moya, "Models of radar clutter from the Weibull distribution," in *Proc. 5th Int. Conf. Signal Process., Robot. Automat. (WSEAS)*, Feb. 2006, pp. 376–380.
[30] H. J. Landau, "Maximum entropy and maximum likelihood in spectral estimation," *IEEE Trans. Inf. Theory*, vol. 44, no. 3, pp. 1332–1336, May 1998.
[31] B. Balaji, F. Barbaresco, and A. Decurninge, "Information geometry and estimation of Toeplitz covariance matrices," in *Proc. Int. Radar Conf.*, Oct. 2014, pp. 1–4.
[32] W. M. Boothby, *An Introduction to Differentiable Manifolds and Riemannian Geometry*. New York, NY, USA: Academic, 2002.
[33] P. Gilkey, J. Park, and R. Vazquez-Lorenzo, *Aspects of Differential Geometry I*. San Rafael, CA, USA: Morgan & Claypool, 2015.
[34] P. T. Fletcher, S. Venkatasubramanian, and S. Joshi, "Robust statistics on Riemannian manifolds via the geometric median," in *Proc. IEEE Conf. Comput. Vis. Pattern Recognit.*, Jun. 2008, pp. 1–8.
[35] A. Barachant, S. Bonnet, M. Congedo, and C. Jutten, "Multiclass brain–computer interface classification by Riemannian geometry," *IEEE Trans. Biomed. Eng.*, vol. 59, no. 4, pp. 920–928, Apr. 2012.
[36] W. Zhang and C. Li, "An eigenvalue inclusion set for matrices with a constant main diagonal entry," *Symmetry*, vol. 10, no. 12, pp. 745–754, Dec. 2018.
[37] C. R. MacCluer, "The many proofs and applications of Perron's theorem," *SIAM Rev.*, vol. 42, no. 3, pp. 487–498, Jan. 2000.
[38] F. C. Robey, D. R. Fuhrmann, E. J. Kelly, and R. Nitzberg, "A CFAR adaptive matched filter detector," *IEEE Trans. Aerosp. Electron. Syst.*, vol. 28, no. 1, pp. 208–216, Jan. 1992.
[39] A. Daniilidis, R. Deville, E. Durand-Cartagena, and L. Rifford, "Self-contracted curves in Riemannian manifolds," *J. Math. Anal. Appl.*, vol. 457, no. 2, pp. 1333–1352, Jan. 2018.
[40] M. Oudin, J. Delmas, F. Barbaresco, and L. Lupinski, "Siegel distance-based covariance matrix selection for space-time adaptive processing," in *Proc. IEEE Radar Conf.*, May 2009, pp. 12–16.
[41] J. A. B. Portas and J. R. C. Corredera, "Probability of false alarm of CA-CFAR detector in Weibull clutter," *Electron. Lett.*, vol. 34, no. 8, pp. 806–807, Apr. 1998.

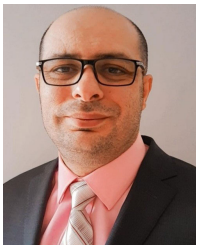

HOSSEIN CHAHROUR (Student Member, IEEE) received the B.Sc. degree in communication engineering with minor in mathematics and the M.Sc. degree in electrical and computer engineering from Carleton University, Ottawa, ON, Canada, in 2006 and 2015, respectively, where he is currently pursuing the Ph.D. degree in electrical and computer engineering. From 2012 to 2015, he was a Research Assistant with the Department of System and Computer Engineering in partnership with Atomic Energy of Canada, Ottawa, and a Defence Scientist with the Defence Research and Development Canada, Ottawa, from 2017 to 2020, and is working with Lockheed Martin Canada. His research interests include all aspects of passive and active radar signal processing, MIMO radar detection and estimation, and information geometry of radar detection.

RICHARD M. DANSEREAU (Senior Member, IEEE) received the B.Sc. and Ph.D. degrees in computer engineering from the University of Manitoba, Winnipeg, MB, Canada, in 1995 and 2001, respectively. From 1996 to 2000, he was a Researcher with Telecommunications Research Laboratories, Winnipeg. From 1999 to 2000, he was with SpectraWorks Inc., Winnipeg. He was also an Instructor for multiple courses with the University of Manitoba, from 1999 to 2000. From 2000 to 2001, he was an Instructor and a Research Engineer with the Department of Electrical and Computer Engineering, Georgia Institute of Technology, Atlanta, GA, USA, where he was with the Center for Signal and Image Processing. Since 2001, he has been a Professor with the Department of Systems and Computer Engineering, Carleton University, Ottawa, ON, Canada, where he was an Associate Chair (Undergraduate Studies), from 2005 to 2007, and an Associate Dean (Student Affairs), from 2015 to 2020. He is currently a Professor with the Faculty of Engineering and Design, Carleton University, and has published more than 100 journal articles and conference papers. His research interests include signal and image processing, biomedical signal processing, sparse signal processing, compressive sensing, source separation, and machine learning for signal processing.

SREERAMAN RAJAN (Senior Member, IEEE) received the B.E. degree in electronics and communications from Bharathiar University, Coimbatore, India, in 1987, the M.Sc. degree in electrical engineering from Tulane University, New Orleans, LA, USA, in 1992, and the Ph.D. degree in electrical engineering from the University of New Brunswick, Fredericton, NB, Canada, in 2004.

From 1986 to 1990, he was the Scientific Officer of the Reactor Control Division, Bhabha Atomic Research Center (BARC), Bombay, India, after undergoing an intense training in nuclear science and engineering from its training school. At BARC, he developed systems for control, safety, and regulation of nuclear research and power reactors. From 1997 to 1998, he carried out research under a grant from Siemens Corporate Research, Princeton, NJ, USA. From 1999 to 2000, he was with JDS Uniphase, Ottawa, ON, Canada, where he worked on optical components and the development of signal processing algorithms for advanced fiber optic modules. From 2000 to 2003, he was with Ceyba Corporation, Ottawa, where he developed channel monitoring, dynamic equalization, and optical power control solutions for advanced ultra-long haul and long haul fiber optic communication systems. In 2004, he was with Biopeak Corporation, where he developed signal processing algorithms for non-invasive medical devices. From December 2004 to June 2015, he was a Defence Scientist with the Defence Research and Development Canada, Ottawa. He was an Adjunct Professor with the School of Electrical Engineering and Computer Science, University of Ottawa, Ottawa, from July 2010 to June 2018. He joined the Department of Systems and Computer Engineering, Carleton University as the Tier 2 Canada Research Chair (Advanced Sensor Systems and Signal Processing), in July 2015, where he is currently a Full Professor. He has been an Adjunct Professor with the Department of Electrical and Computer Engineering, Royal Military College, Kingston, ON, Canada, since July 2015. He is also the Director of Ottawa-Carleton Institute for Biomedical Engineering (OCIBME). He is the holder of two patents and two disclosures of invention. He has published more than 175 journal articles and conference papers. His research interests include signal and image processing, biomedical signal processing, pattern classification, and applied machine learning. He has served the IEEE Canada as its Board Member, for the period 2010–2018 and is the Chair of the IEEE Ottawa EMBS and AESS Chapters. He was awarded the IEEE MGA Achievement Award, in 2012, and recognized for his IEEE contributions with Queen Elizabeth II Diamond Jubilee Medal, in 2012. IEEE Canada recognized his outstanding service through the 2016 W. S. Read Outstanding Service Award. He has been involved in organizing several successful IEEE conferences and has been a reviewer of several IEEE journals and conferences.

BHASHYAM BALAJI (Senior Member, IEEE) received the B.Sc. degree (Hons.) in physics from St. Stephen's College, University of Delhi, New Delhi, India, in 1990, and the Ph.D. degree in theoretical particle physics from Boston University, Boston, MA, USA, in 1997. Since 1998, he has been a Defence Scientist with the Defence Research and Development Canada, Ottawa, ON, Canada. His research interests include all aspects of radar sensor outputs, including space-time adaptive processing, multitarget tracking, and meta-level tracking, as well as multisource data fusion. His theoretical research interests also include the application of Feynman path integral and quantum field theory methods to the problems of nonlinear filtering and stochastic control. Most recently, his research interests have included quantum sensing, in particular, quantum radar and quantum imaging. He is a fellow of the Institution of Engineering and Technology. He was a recipient of the IEEE Canada Outstanding Engineer Award, in 2018.